nature physics

Article

https://doi.org/10.1038/s41567-022-01839-x

Non-thermal electron acceleration from magnetically driven reconnection in a laboratory plasma

Received: 11 June 2021

Accepted: 14 October 2022

Published online: 16 January 2023

Check for updates

Abraham Chien[1] ✉, Lan Gao[2], Shu Zhang[1], Hantao Ji[1,2] ✉, Eric G. Blackman[3,4], William Daughton[5], Adam Stanier[5], Ari Le[5], Fan Guo[5], Russ Follett[4], Hui Chen[6], Gennady Fiksel[7], Gabriel Bleotu[8,9,10], Robert C. Cauble[6], Sophia N. Chen[8], Alice Fazzini[10], Kirk Flippo[5], Omar French[2,11], Dustin H. Froula[4], Julien Fuchs[10], Shinsuke Fujioka[12], Kenneth Hill[2], Sallee Klein[7], Carolyn Kuranz[7], Philip Nilson[4], Alexander Rasmus[5] & Ryunosuke Takizawa[12]

Magnetic reconnection rapidly converts magnetic energy into some combination of plasma flow energy, thermal energy and non-thermal energetic particles. Various reconnection acceleration mechanisms have been theoretically proposed and numerically studied in different collisionless and low-β environments, where β refers to the plasma-to-magnetic pressure ratio. These mechanisms include Fermi acceleration, betatron acceleration, parallel electric field acceleration along magnetic fields and direct acceleration by the reconnection electric field. However, none of them have been experimentally confirmed, as the direct observation of non-thermal particle acceleration in laboratory experiments has been difficult due to short Debye lengths for in situ measurements and short mean free paths for ex situ measurements. Here we report the direct measurement of accelerated non-thermal electrons from magnetically driven reconnection at low β in experiments using a laser-powered capacitor coil platform. We use kilojoule lasers to drive parallel currents to reconnect megagauss-level magnetic fields in a quasi-axisymmetric geometry. The angular dependence of the measured electron energy spectrum and the resulting accelerated energies, supported by particle-in-cell simulations, indicate that the mechanism of direct electric field acceleration by the out-of-plane reconnection electric field is at work. Scaled energies using this mechanism show direct relevance to astrophysical observations.

Magnetic reconnection, the process by which magnetic field topology in a plasma is reconfigured, rapidly converts magnetic energy into some combination of bulk flow and thermal and non-thermal energetic particles[1,2]. The latter is a prominent feature of presumed reconnection regions in nature, and as such, reconnection can be thought of as an efficient particle accelerator in low-β ($\lesssim$1) collisionless plasmas where abundant magnetic free energy per particle is available (β refers to the plasma-to-magnetic pressure ratio). Electron acceleration up

A full list of affiliations appears at the end of the paper. ✉e-mail: achien@princeton.edu; hji@pppl.gov

https://doi.org/10.1038/s41567-022-01839-x

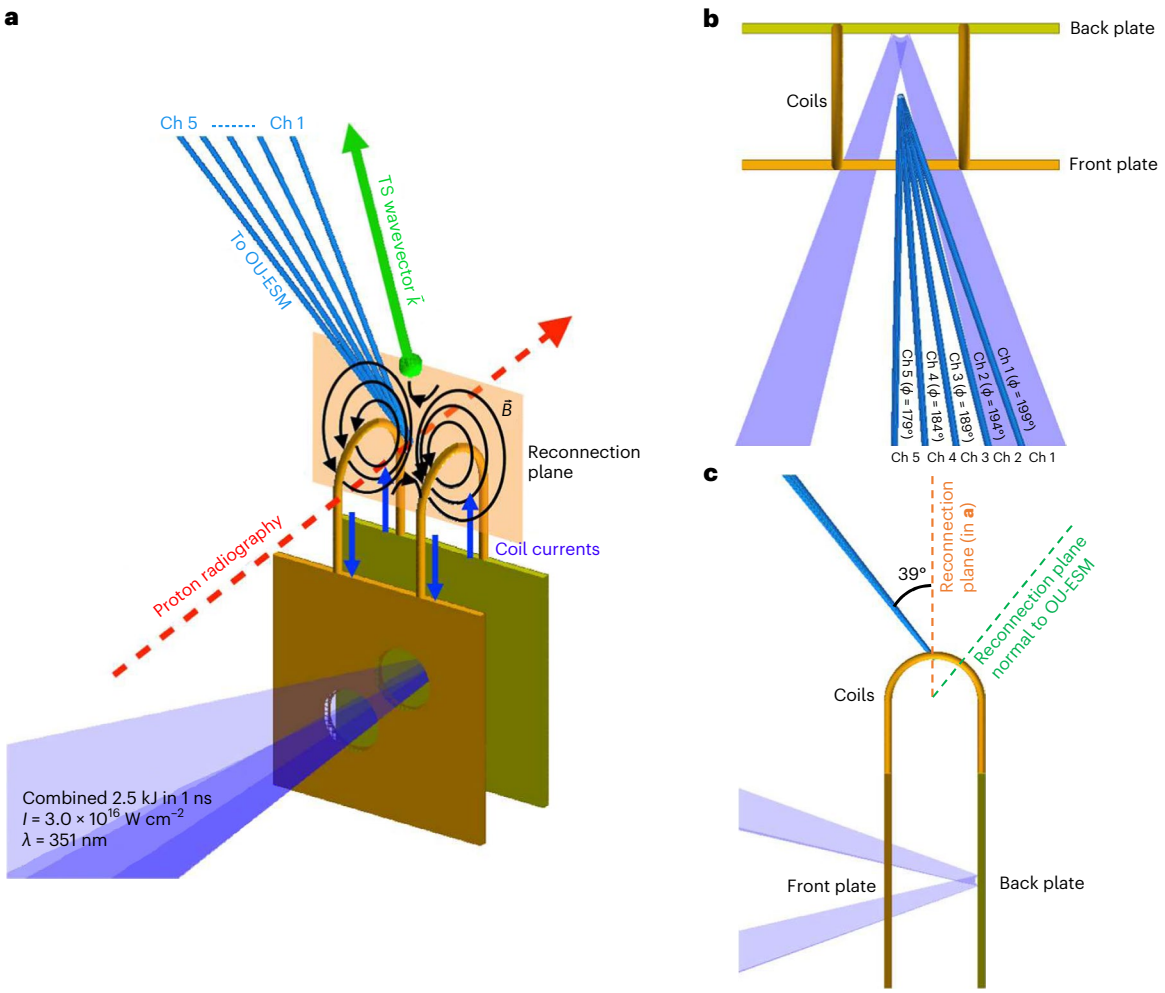

Fig. 1 | Experimental setup of magnetically driven reconnection at low β. a, Capacitor coil target is driven by two long-pulse lasers, passing through the front holes and irradiating the back plate. An electrostatic potential is created between the (capacitor) plates, and large currents (blue arrows) are generated in the parallel U-shaped coils. The resulting magnetic fields form a reconnection structure between the coils. Major diagnostics are target normal sheath acceleration proton radiography, indicated by the red dashed arrow, and the OU-ESM that is positioned 37.5 cm away from the main interaction at an angle of 39° from the vertical. Five independent channels (their directions are indicated by the blue solid lines) are situated within 5° between each channel, allowing a measurement of the angular spread of electrons in the azimuthal direction. Thomson scattering measurements were taken in a similar experiment[39] to diagnose plasma parameters: the green ball shows the probing volume, and the Thomson scattering wavevector $\vec{k}$ is also shown. **b**, Top-down view of the main target is shown, along with the OU-ESM channel orientation in the azimuthal direction. The azimuthal origin ($\phi = 0°$) corresponds to the direction normal to the back plate, extending away from the front plate. The left and right coils are defined with respect to the top-down view. **c**, Side-on view of the main target shows the relative polar orientation of the OU-ESM channels. The orange vertical dashed line represents the reconnection plane shown in **a**, and the green dashed line represents the reconnection plane that is normal to the OU-ESM line of sight. Due to the generation of a strong LPI signal by the short-pulse laser for proton radiography, electron spectral measurements are taken in the absence of proton radiography.

to ~300 keV, for example, has been observed in Earth's magnetotail[3] and the measured spectra in X-ray, extreme-ultraviolet and microwave wavelengths from solar flares include a non-thermal power law component, indicating a large suprathermal electron population[4–6]. Reconnection has been suggested as the underlying source of these non-thermal electrons. Gamma-ray flares from the Crab nebula are another example, exhibiting particle acceleration up to 10^{15} eV, which cannot be explained by shock acceleration mechanisms[7–9].

The efficient acceleration of charged particles by magnetic reconnection[10,11] has been theoretically and numerically[12–19] studied, and various acceleration mechanisms including direct acceleration by the reconnection electric field[20], parallel electric field acceleration[21], Fermi acceleration[22] and betatron acceleration[23] have been proposed. However, thus far, no direct measurements of non-thermal particle acceleration due to reconnection at low β have been made in laboratory experiments to confirm or contradict these mechanisms. Short Debye lengths and mean free paths have limited most in situ and ex situ detection of the predicted energetic electrons, respectively, whereas the indirect measurements of energetic electrons are necessarily limited by specific models assumed for radiation and acceleration mechanisms[24–26].

High-energy-density plasmas[27–36] have recently emerged as novel platforms to study magnetic reconnection. In particular, direct measurements of charged particle spectra are possible due to a large electron mean free path relative to the detector distance. Importantly, low-β, collisionless, magnetically driven reconnection is achievable using laser-powered capacitor coils[32–34], allowing relevant conditions to astrophysical environments. Here, using this experimental reconnection platform, we directly detect non-thermal electron acceleration from reconnection, and combined with particle-in-cell (PIC) simulations, infer a primary acceleration mechanism of direct electric field acceleration by the reconnection electric field.

https://doi.org/10.1038/s41567-022-01839-x

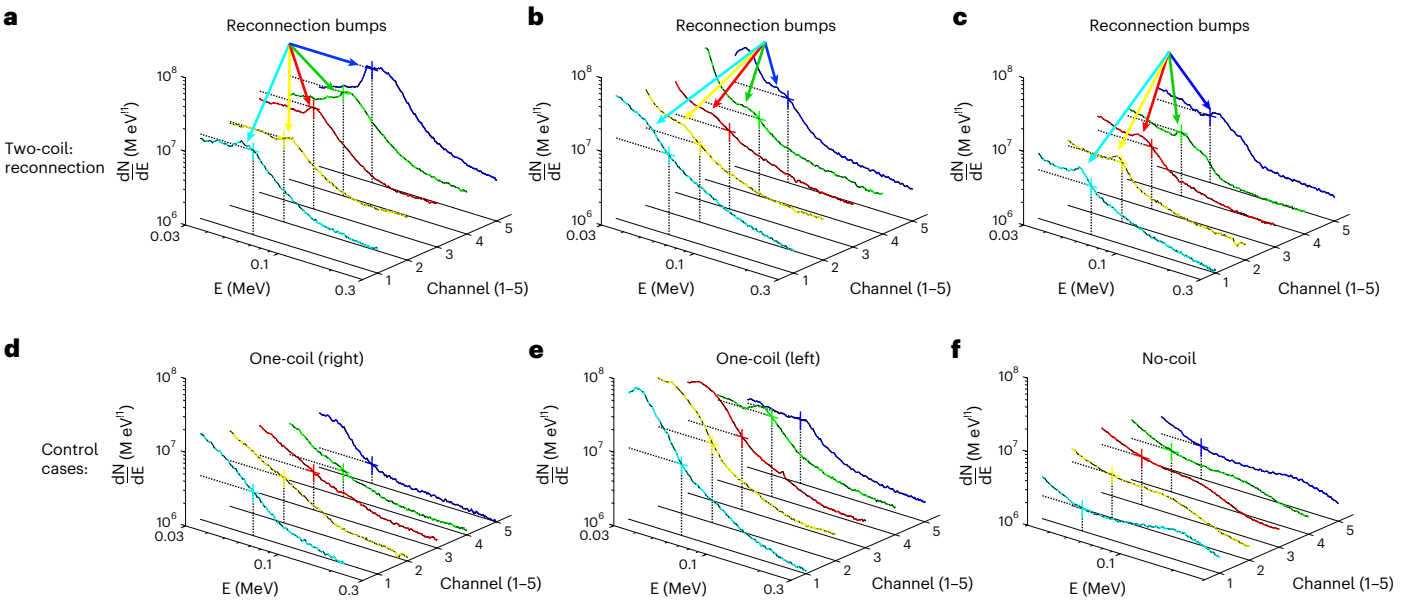

Fig. 2 | Experimental evidence of non-thermal electron acceleration. **a**–**f**, Particle energy spectra (*x* axis, MeV; *y* axis, number of particles) from the OU-ESM are presented for six experimental shots: three two-coil reconnection cases (**a**–**c**), two one-coil control cases (**d** and **e**) and one no-coil control case (**f**). The right (**d**) and left (**e**) coils are defined with respect to the top-down view shown in Fig. 1b. Five colours represent the five channels spread in the azimuthal angle (Fig. 1b). In all the plots, a cross represents the characteristic horizontal and vertical error bars at $E = 60$ keV. The horizontal errors are in terms of particle energy, propagated from the uncertainty in image-plate position relative to the magnets. The vertical errors are in terms of number of particles, propagated from the sensitivity uncertainties of the image plate. The dashed lines serve as visual aids. Despite shot-to-shot variations in the signal level, in the reconnection cases, spectral bumps are observed in the 40–70 keV range. These bumps are significant and observed to exceed the experimental signal error. They are the strongest in channel 5, representing a near-face-on view of the target, and decrease with larger azimuthal angle, with the weakest bumps in channel 1, representing 19° off normal. Such a trend is noticeably absent in the control cases, where overall weaker signal levels are observed. A feature appearing to be a spectral bump is observed in **e**, but it is, in fact, a deficiency in the low-energy range: due to the coil position on the left, low-energy electrons are preferentially deflected towards the direction of the right coil (large θ–z pitch angle), resulting in an absence in channels 4 and 5. This behaviour is supported by ray-tracing simulations (Methods and Extended Data Fig. 1c). The no-coil control case (**f**) exhibits a much lower signal level than the one-coil control cases and reconnection cases, implying the magnetic field from the coils is deflecting hot electrons towards the detector.

Our experiments using laser-powered capacitor coils were performed at the OMEGA Extended Performance (EP) facility at the Laboratory for Laser Energetics. The experimental setup, with diagnostic locations, is shown in Fig. 1. The capacitor coil target is driven with two laser pulses, each delivering 1.25 kJ of laser energy in a 1 ns square temporal profile at a wavelength of 351 nm. The corresponding on-target laser intensity is ~3×10^{16} W cm^{-2}. Due to the laser interaction, strong currents are driven in the coils. In targets with two parallel coils, a magnetic reconnection field geometry is created between the coils, and in targets with one coil, a simple magnetic field around a wire is produced, as well as in targets with no coils, representing a non-reconnection control case. Further information on capacitor coil target operation and design are provided in Methods.

The coil current profile can be approximated by a linear rise during the laser pulse ($0 < t < t_{rise}$), followed by an exponential decay after the laser is turned off. Target normal sheath acceleration[37] proton radiography measurements indicated a maximum coil current of 57 kA at $t_{rise} = 1$ ns, corresponding to a magnetic field of 110 T at the centre of the coils and an upstream reconnection magnetic field strength of 50.7 T, with a subsequent exponential decay time of $t_{decay} = 8.6$ ns (ref. 33). During the current rise, the magnetic field strengthens, driving a 'push'-phase reconnection, where field lines are pushed into the reconnection region, and during current decay, 'pull' reconnection occurs, where field lines are pulled out of the reconnection region[38]. Due to the short timescale of the push phase relative to the pull phase, reconnection is more strongly driven during the push phase, and the push phase is the dominant source of particle acceleration.

We used Thomson scattering to diagnose the reconnecting copper plasma in a similar experiment on the OMEGA laser[39], and found electron density $n_e \simeq 3 \times 10^{18}$ cm^{-3}, ion density $n_i \simeq 1.7 \times 10^{17}$ cm^{-3} and electron and ion temperatures $T_e \simeq T_i \simeq 400$ eV. Due to the large $Z = 18$, the ion plasma pressure is negligible compared with the electron plasma pressure, and the ratio of plasma pressure to magnetic pressure $\beta \simeq 0.05$. The experiments are, therefore, firmly in the low-β regime, most pertinent for particle acceleration in astrophysical conditions. The Lundquist number is 10^3–10^4, representing collisionless reconnection. The reconnection system size is defined by the intercoil distance of $L = 600$ μm, and when normalized by the ion skin depth d_i, the normalized system size $L/d_i \simeq 1.4$. Due to the small system size, the reconnection is deeply in the electron-only regime[40], where ions are decoupled.

A time-integrated electron spectrometer—the Osaka University electron spectrometer (OU-ESM)—was used to measure the electron energy spectra. It is located 37.5 cm away from the coils, at a polar angle of 39° and scans an azimuthal range of 179°–199° with five equally spaced detection channels. The OU-ESM channel orientation is shown in Fig. 1b,c. During OU-ESM measurements, the short-pulse beam driving the target normal sheath acceleration proton radiography was turned off to avoid noise due to laser–plasma instabilities (LPI) from the short-pulse interaction. Further details regarding the OU-ESM are given in Methods. Figure 2 shows the experimentally measured OU-ESM data for three double-coil reconnection shots as well as two single-coil and one no-coil control shots. Although neither one-coil nor no-coil shots represent perfect control cases, the combination of these configurations allows for better isolation of the reconnection signal.

https://doi.org/10.1038/s41567-022-01839-x

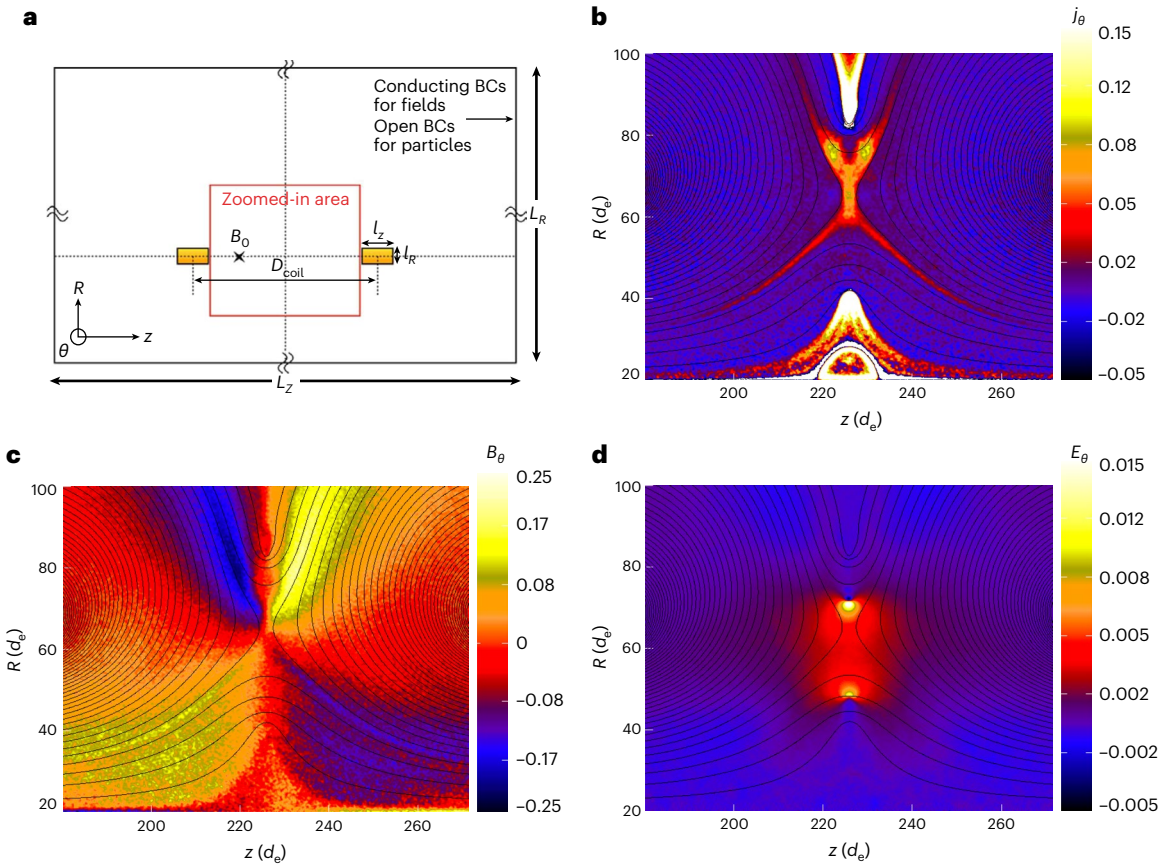

Fig. 3 | PIC simulation setup and results. a, Schematic of the 2D cylindrical simulation box used in VPIC modelling, where z is the axis of symmetry and R is the radial direction. Here L_z and L_R are the box sizes. The azimuthal angle θ is directed out of the page. Two rectangular coils, each with a cross section of l_z and l_R, are situated at $R = R_{coil}$ with centre-to-centre separation of D_{coil}. The reference magnetic field B_0 is measured upstream from the coils. Conducting boundary conditions (BCs) for fields and open-boundary conditions for the particles are stipulated. The current is injected in the coils with time, replicating the experimental current profile. Time evolution of fields are evaluated relative to the current rise time t_{rise}, to keep the magnetic field drive consistent. All the measurements are taken in the zoomed-in box area (marked in red). The outer box boundary is not to scale. **b**–**d**, The 2D profiles of out-of-plane electric current density j_θ, out-of-plane magnetic field B_θ and reconnection electric field E_θ in the red rectangular zoomed-in area of the (R, z) plane are shown at $t = 1.55t_{rise}$, overlaid with magnetic field lines. B_θ shows a characteristic quadrupole field structure from decoupled electron and ion flows. A noticeable reconnection electric field is observed around the current sheet near the magnetic null, with the orientation indicating push reconnection. j_θ, B_θ and E_θ are shown in the respective normalized units: $j_0 = en_{e0}c$, $B_0 = m_e\omega_{pe}/e$ and $E_0 = cB_0 = m_e\omega_{pe}c/e$.

Small differences in the laser energy profile and target properties among shots causes variations in otherwise nominally identical cases (Fig. 2). However, focusing on the angular dependence across the channels for each shot reveals a key feature in the electron spectra: non-thermal 'bumps' in the reconnection cases that do not appear in the control cases. The bumps span the 40–70 keV range, and they are the most pronounced at the near-normal channel 5 ($\phi = 179°$) and weaken with an increasing angle from normal. In contrast, the one-coil control cases do not exhibit consistent spectral bumps, and generally exhibit a lower signal level. One exception is shown in Fig. 2e—a one-coil shot with the coil on the left side (as viewed from the front of the target). Due to the coil magnetic field, low-energy electrons are deflected towards higher ϕ, resulting in an electron deficiency in channel 5 and to a lesser extent in channel 4. The no-coil control case exhibits an even lower signal level than the one-coil case: this is due to the lack of a magnetic field to deflect electrons towards the detector. The background 'thermal' signal does not represent the $T_e = 400$ eV plasma: it is the quasi-Maxwellian suprathermal distribution with a hot 'temperature' of $T_{e,h} \simeq 40$–50 keV, created by LPI, such as stimulated Raman scattering and two-plasmon decay[41–43].

These spectral bumps demonstrate non-thermal electron acceleration, and the detection angle dependence of the bump sizes suggests directional anisotropy in the accelerated electron population. The strongest non-thermal population is seen in the direction out of the reconnection plane, anti-parallel to the reconnection electric field, indicating its responsibility for direct acceleration[20,44,45].

Interpretation of this particle acceleration mechanism is supported by PIC simulations. We conducted two-dimensional (2D) cylindrical PIC simulations using the Vector Particle-In-Cell (VPIC) code[46] to model the kinetic effects and simulated particle energy spectra (Fig. 3a shows the geometric setup). The z direction is the axis of symmetry, R is the radial direction and θ is the out-of-plane direction. Two rectangular-cross-section coils are placed in the simulation box, representing cross-sectional slices of the experimental U-shaped coils. Reconnection is driven by prescribing and injecting currents within the coils. We prioritize the realistic mass ratio and β in the simulation, at the expense of the reduced but scaled ratio of electron plasma frequency to electron gyrofrequency, ω_{pe}/Ω_{ce}, due to limited computational resources. Further details for the simulation setup are described in Methods.

The PIC simulation results demonstrate strong reconnection driven by the coil magnetic fields, with a typical out-of-plane quadrupole structure (Fig. 3c), indicative of scale separation between the ions and electrons[47,48]. In addition, a clear out-of-plane reconnection electric

https://doi.org/10.1038/s41567-022-01839-x

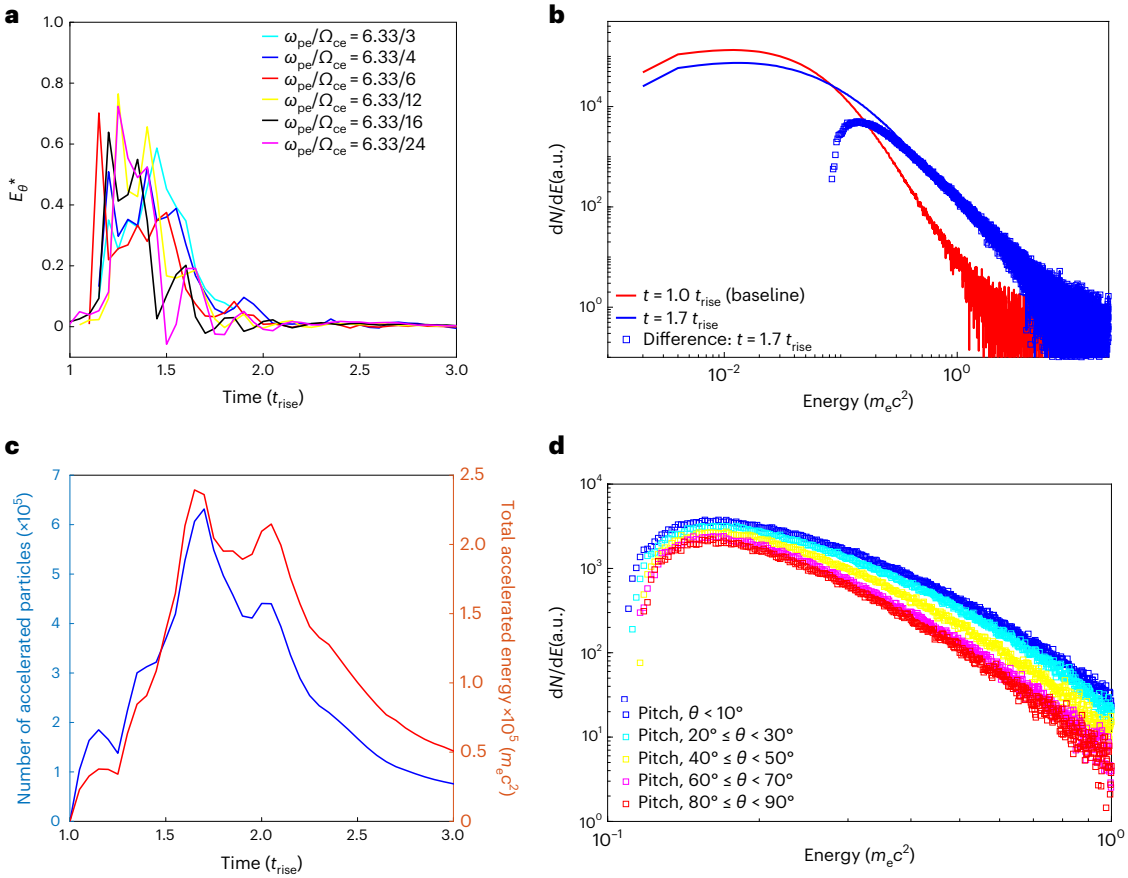

Fig. 4 | Simulations validate electron acceleration mechanism. a, Normalized electric field, or reconnection rate, E_θ^*, is obtained by dividing the reconnection electric field by the upstream $V_A \times B_0$, where V_A is the Alfvén speed computed with the upstream magnetic field B_0 and ion mass density in the reconnection region. From the period of $t \approx (1–2)t_{rise}$, where t_{rise} is the current rise time, the reconnection electric field is prominent. E_θ^* is generally constant across the ω_{pe}/Ω_{ce} scan, representing consistent reconnection physics. **b**, Electron number particle spectrum is measured within the zoomed-in box (Fig. 3) and with limiting the θ–z pitch angle to 10°. The particle spectrum for ω_{pe}/Ω_{ce} = 6.33/4 is shown: $t \approx 1.0t_{rise}$ (red) represents the baseline spectrum. The maximum non-thermal tail is seen at $t \approx 1.7t_{rise}$, consistent with the time dependence of the reconnection electric field. The non-thermal difference from the baseline spectrum is shown in blue squares. **c**, Number of accelerated electrons (blue; measured by the non-thermal difference against the baseline) and the total energy of the accelerated electrons (red) are plotted as a function of time. The peak acceleration occurs at $t \approx 1.7t_{rise}$, largely consistent with the time of maximum reconnection electric field. The subsequent decay in accelerated electron count and accelerated energy is attributed to the stopping of the reconnection process and effect of the open-boundary conditions. **d**, Non-thermal difference spectra are shown for $t = 1.7t_{rise}$, separated by θ–z pitch angle. Small pitch angles (near normal to the reconnection plane) correspond to higher-energy tails, whereas large pitch angles (near parallel to the reconnection plane) show smaller non-thermal acceleration.

field is observed around the X point, and the orientation of the electric field is consistent with push reconnection (Fig. 3d).

To obtain the reconnection rate, the reconnection electric field is typically normalized by an upstream $V_A B_0$, where B_0 is the upstream magnetic field strength and $V_A = B_0/\sqrt{\mu_0 m_i n_i}$ is the Alfvén velocity calculated with the ion density at the X point. Figure 4a shows that the strongest reconnection occurs from $t \approx t_{rise} - 1.7t_{rise}$, for all the simulated values of ω_{pe}/Ω_{ce}. The diffusion time of the magnetic field through the plasma explains why this timing does not correspond to the expected period of push reconnection at $t < t_{rise}$. In nearly all cases, the reconnection rate reaches the maximum values of 0.6–0.7, much higher than the typical ~0.1 rate expected for collisionless electron–ion reconnection[49]: this is typical of electron-only reconnection, which is characterized by a normalized system size[50] of $L/d_i \lesssim 5$.

Since the reconnection rate is constant across the ω_{pe}/Ω_{ce} scan, we estimate the reconnection electric field in physical units as $E_{rec} \simeq 0.6 V_A B_0$, where 0.6 is the reconnection rate (Fig. 4a). Taking B_0 = 50.7 T and a range of $n_e = 1–5 \times 10^{18}$ cm^{-3}, $E_{rec} \simeq 1.3–3.0 \times 10^7$ V m^{-1}. This value is consistent with fitting a power law of index $k = -2.137$ to the reconnection electric field strength as a function of ω_{pe}/Ω_{ce}.

Electromagnetic fields from the PIC simulations are analysed through a synthetic proton ray-tracing algorithm to predict a dark-centre feature corresponding to the reconnection current sheet during push reconnection. This centre feature is observed in experimental proton radiographs taken at t = 1.0 ns after the laser pulse (Fig. 5e), indicating the presence of reconnection in the experimental platform. To generate the synthetic proton radiograph, protons with a kinetic energy of 50 MeV are advanced via a fourth-order Runge–Kutta algorithm. At each proton position, electromagnetic fields are inferred from the 2D PIC fields, 'swept' in angle along the semicircular portion of the coils. More details of the synthetic ray-tracing algorithm are described in Methods.

Synthetic ray tracing is performed for $t = 1.4t_{rise}$, corresponding to a strong push reconnection. The centre feature is reproduced in the radiograph (Fig. 5b), and two primary features in the out-of-plane current j_θ profiles (Fig. 5a) are potentially responsible for creating this centre feature: the push reconnection current sheet and diamagnetic

https://doi.org/10.1038/s41567-022-01839-x

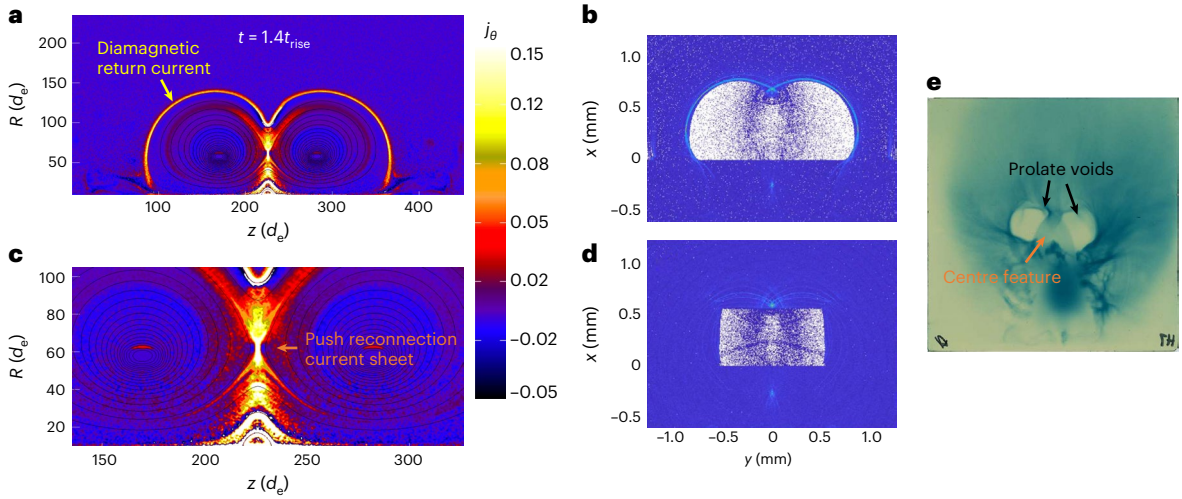

Fig. 5 | Centre feature in proton radiographs reproduced synthetically. a–d, Full box (**a**; Fig. 3) and zoomed-in 2D profiles (**c**) in the (R, z) plane of the out-of-plane current j_θ in the normalized unit of $j_0 = en_{e0}c$ with the respective synthetic proton radiographs (**b** and **d**) for $t = 1.4t_{rise}$, where t_{rise} is the current rise time. The synthetic proton radiographs are generated by 'sweeping' the electromagnetic field structure in a semicircle, advancing a cone of protons by ray tracing through the fields in the z direction, and recording the projected proton positions in the y–x plane. The diamagnetic return current can be seen in the full j_θ profile, but not in the zoomed-in profile. **e**, Experimental proton radiograph taken at $t = 1.0$ ns and proton energy $E_p = 18.3$ MeV. Two primary features are seen: two prolate voids are caused by the coil magnetic fields, and the centre feature can be explained by electromagnetic fields corresponding to a push reconnection current sheet. In the synthetic radiographs, the white areas represent no proton fluence, the dark blue areas represent the background proton level and the bright blue areas represent the highest proton concentration. In the experimental radiograph, the white areas represent no proton fluence and the darker shades of green represent larger proton concentrations.

Table 1 | Comparisons of maximum electron energy from observation and their estimation

Low-β plasma	Size, L (m)	n_e (m^{-3})	B (T)	$E_{max,obs}$ (eV)	$E_{max,est}$(eV)	Notes or assumptions
Laser plasma (this work)	1×10^{-3}	1×10^{24}	50	$(4–7)\times10^{4}$	3×10^{4}	Cu^{+18} plasma
Magnetotail[3]	6×10^{8}	1×10^{5}	1×10^{-8}	3×10^{5}	4×10^{5}	In situ measurement
Solar flares[54,55]	1×10^{7}	1×10^{15}	2×10^{-2}	1×10^{8}	6×10^{10}	
X-ray binary disk flares[56,57]	3×10^{4}	1×10^{24}	1×10^{4}	5×10^{8}	1×10^{14}	Cygnus X-3, $M=10M_\odot$, $R=R_S$
Crab nebula flares[7–9]	1×10^{17}	10^{6}	1×10^{-8}	5×10^{15}	2.4×10^{15}	Pair plasma
Gamma-ray bursts[44,58]	10^{4}	2×10^{35}	4×10^{9}	5×10^{9}	3×10^{20}	Pair plasma
Magnetar flares[59]	10^{4}	10^{41}	2×10^{11}	2×10^{8}	5×10^{20}	Pair plasma, FRB 121102
AGN disk flares[56,60]	3×10^{11}	1×10^{17}	4	5×10^{8}	3×10^{17}	Seyfert 1 NGC 5548, $M=10^8M_\odot$, $R=R_S$
Radio lobes[61]	3×10^{19}	0.1	5×10^{-10}	5×10^{11}	5×10^{16}	
Extragalactic jets[62]	3×10^{19}	3×10^{1}	10^{-7}	7×10^{12}	1×10^{18}	3C 303

The observations are from low-β reconnection sources, as a partial list from another work[51], and their estimation is based on reconnection electric field acceleration of $0.1V_ABd$. Here d is the characteristic acceleration distance that is taken to be the system size for maximum energy. Unless explicitly stated, plasmas consist of electrons and protons.

return current. To deconvolve the effects of each on the synthetic proton radiographs, ray tracing is performed on a 'zoomed-in' field, where the diamagnetic return current is largely shielded out (Fig. 5c). The centre feature is maintained in this radiograph (Fig. 5d), indicating the source of the centre feature as the push reconnection current sheet. Thus, the presence of a similar centre feature in experimental radiographs is indicative of push reconnection and the corresponding electromagnetic fields.

Finally, the PIC simulations demonstrate non-thermal particle acceleration during the push phase of reconnection. Various filters are applied to the electron population to select the electrons that best compare with the experimental spectra. First, to focus on the electrons that are affected by reconnection, electrons are measured only within the zoomed-in simulation area (Fig. 3a). Second, the θ–z pitch angle is limited to select electrons that can escape and be measured by the OU-ESM detector. For our 2D axisymmetric simulation, we do not limit the θ–R pitch angle, since for any fixed detector angle and θ–R pitch angle, a reconnection plane exists such that a particle accelerated from that plane would reach the detector.

Due to the particle injection scheme from $0 < t < t_{rise}$, the baseline spectrum is taken at $t = t_{rise}$, to distinguish reconnection-accelerated electrons from the injected electrons. The reconnection rate evolution shows that reconnection does not begin until $t > t_{rise}$, further validating this approach. Figure 4b shows the formation of a non-thermal electron tail. The tail grows larger with time, up to a maximum (at $t \approx 1.7t_{rise}$), and begins to decay back to a Maxwellian, as reconnection stops and accelerated particles escape the system through the open boundaries. The number of electrons in the tail and energy content of the tail

are observed to peak at $t \approx 1.7t_{rise}$ (Fig. 4c). The time of the maximally non-thermal spectrum corresponds well to the time dependence of the reconnection electric field, demonstrating push reconnection as the source of accelerated particles.

A comparison of the experimental particle spectra with PIC simulations supports acceleration by the reconnection electric field as the primary acceleration mechanism that forms the non-thermal electron tail. This is evidenced by the angular dependence and accelerated energies of the non-thermal tails in experimental measurements. The strongest non-thermal components are seen in channel 5, corresponding to its near-normal orientation. The strength of the bump decreases as the azimuthal angle grows more oblique. Acceleration by the out-of-plane reconnection electric field would be expected to produce this angular dependence: electrons with larger pitch angles would be directed into regions with high field, resulting in re-magnetization, preventing the electron from reaching the detector. This angular dependence of the accelerated electrons is confirmed by PIC simulations (Fig. 4d), where non-thermal electrons decrease with increasing pitch angle from the reconnection electric field direction.

Other proposed acceleration mechanisms are not expected to be applicable because the required conditions for them are not satisfied in our experiment. Fermi acceleration typically requires multiple plasmoids in the current sheet as acceleration sites. Parallel electric field acceleration requires a finite guide field. Betatron acceleration requires increasing magnetic field in the downstream region. Polarization drift acceleration is unimportant for electrons.

Although the accelerated particle spectrum from simulations could not be obtained for the experimental value of $\omega_{pe}/\Omega_{ce} = 6.33$ through scaling due to a prohibitive computational cost (Methods), the simulation-determined scaling of the out-of-plane electric field is well established. Using the calculated reconnection electric field $E_\theta = (1.3–3.0) \times 10^7$ V m^{-1}, a simple estimate for the expected accelerated electron energy gain becomes $\Delta E \approx |q_e| E_\theta d$, where q_e is the electron charge and d is a characteristic acceleration distance (here $d \approx 1{,}000$ μm). This predicts 13–30 keV electrons, which represents an upper bound on the accelerated electron energy with this mechanism, and is within a factor of 2 of the experimental bump of ~40–70 keV. Several potential factors can explain this discrepancy. First, a larger reconnection electric field and thus larger electron acceleration can be achieved with a larger than expected upstream magnetic field or a smaller than expected plasma density since $E_\theta \propto V_A$. The former can occur due to magnetic field pileup in the upstream region. Plasma density near the X point is uncertain because the Thomson scattering probes the plasma located in the downstream region above the coils.

Second, there is a possibility that the bump may not be due to reconnection: instead, due to the different magnetic geometries of the reconnection and one-coil cases, LPI-generated electrons of certain energies may be preferentially deflected towards certain angles, contributing to the observed spectral bump. This possibility is analysed in detail using electron/positron ray tracing with vacuum magnetic fields from the coils (Methods), and the ray-tracing results show that this coil magnetic field deflection alone is unable to reproduce the experimentally observed bumps in the reconnection cases. Plasma effects in the ray-tracing simulations are expected to be small, as illustrated by the low signal level in the no-coil electron spectra (Fig. 2f). This further supports that the detected electron spectral bump is due to reconnection.

The inference that direct electric field acceleration is operating in the experiments motivates estimating the corresponding attainable particle energies from this mechanism in representative low-β collisionless reconnecting plasmas throughout the Universe[51] and comparing with the maximum inferred electron energies from observations. The result is shown in Table 1, where we have assumed that our experimental implications for the mostly electron-only reconnection regime can be extended to electron–ion or pair-plasma reconnection regimes. This leads to the reconnection electric field $E_\theta = 0.1 V_A B$ typically found in collisionless reconnection[49]. Therefore, the upper bound for the energy of the accelerated electrons by the reconnection electric field is established by the Hillas limit[52] as $E_{max,est} = eE_\theta d$, where d is a characteristic acceleration distance (taken here to be the system size L).

The estimated maximum energy is within a factor of 2 for Earth's magnetotail and Crab nebula flares, implying that if this mechanism is responsible for acceleration of the most energetic electrons in these two cases, coherent acceleration over a distance comparable to the system size is required. In all the other cases, the observed maximum electron energy is well below the estimated theoretical maximum energy, suggesting that if this mechanism is at work, it must operate over length scales much shorter than the system size but with a properly distributed spread to populate the whole electron energy spectrum. Interestingly, this scaling of maximum energy has also been identified in large-scale simulations at low β but in relativistic regimes[53].

Our laser-powered capacitor coils offer a unique experimental reconnection platform in magnetically driven low-β plasmas to further study the acceleration of electrons (and ions) in various reconnection regimes[2,51] via the direct detection of accelerated particles. The extent to which the same or different mechanisms[10,11] of particle acceleration emerge in different regimes will be of great interest to determine by laboratory research in the future and may depend on the particular reconnection boundary conditions and system geometries. Although no other mechanisms are excluded, our reported results serve as direct evidence of any hypothesized acceleration mechanism by magnetic reconnection.

Online content

Any methods, additional references, Nature Portfolio reporting summaries, source data, extended data, supplementary information, acknowledgements, peer review information; details of author contributions and competing interests; and statements of data and code availability are available at https://doi.org/10.1038/s41567-022-01839-x.

References

1. Yamada, M., Kulsrud, R. & Ji, H. Magnetic reconnection. *Rev. Mod. Phys.* **82**, 603–664 (2010).
2. Ji, H. et al. Magnetic reconnection in the era of exascale computing and multiscale experiments. *Nat. Rev. Phys.* **4**, 263–282 (2022).
3. Øieroset, M., Lin, R. P., Phan, T. D., Larson, D. E. & Bale, S. D. Evidence for electron acceleration up to ~300 keV in the magnetic reconnection diffusion region of Earth's magnetotail. *Phys. Rev. Lett.* **89**, 195001 (2002).
4. Masuda, S., Kosugi, T., Hara, H., Tsuneta, S. & Ogawara, Y. A loop-top hard X-ray source in a compact solar flare as evidence for magnetic reconnection. *Nature* **371**, 495–497 (1994).
5. Krucker, S. et al. Measurements of the coronal acceleration region of a solar flare. *Astrophys. J.* **714**, 1108–1119 (2010).
6. Chen, B. et al. Measurement of magnetic field and relativistic electrons along a solar flare current sheet. *Nat. Astron.* **4**, 1140–1147 (2020).
7. Tavani, M. et al. Discovery of powerful gamma-ray flares from the Crab nebula. *Science* **331**, 736–739 (2011).
8. Abdo, A. et al. Gamma-ray flares from the Crab nebula. *Science* **331**, 739–742 (2011).
9. Kroon, J. J., Becker, P. A., Finke, J. D. & Dermer, C. D. Electron acceleration in pulsar-wind termination shocks: an application to the Crab nebula gamma-ray flares. *Astrophys. J.* **833**, 157 (2016).
10. Blandford, R., Yuan, Y., Hoshino, M. & Sironi, L. Magnetoluminescence. *Space Sci. Rev.* **207**, 291–317 (2017).
11. Guo, F. et al. Recent progress on particle acceleration and reconnection physics during magnetic reconnection in the magnetically-dominated relativistic regime. *Phys. Plasmas* **27**, 080501 (2020).

12. Drenkhahn, G. & Spruit, H. C. Efficient acceleration and radiation in Poynting flux powered GRB outflows. *Astron. Astrophys.* **391**, 1141–1153 (2002).
13. Sironi, L. & Spitkovsky, A. Relativistic reconnection: an efficient source of non-thermal particles. *Astrophys. J. Lett.* **783**, L21 (2014).
14. Dahlin, J. T., Drake, J. F. & Swisdak, M. The mechanisms of electron heating and acceleration during magnetic reconnection. *Phys. Plasmas* **21**, 092304 (2014).
15. Werner, G. R., Uzdensky, D. A., Cerutti, B., Nalewajko, K. & Begelman, M. C. The extent of power-law energy spectra in collisionless relativistic magnetic reconnection in pair plasmas. *Astrophys. J. Lett.* **816**, L8 (2016).
16. Dahlin, J. T., Drake, J. F. & Swisdak, M. Parallel electric fields are inefficient drivers of energetic electrons in magnetic reconnection. *Phys. Plasmas* **23**, 120704 (2016).
17. Totorica, S. R., Abel, T. & Fiuza, F. Nonthermal electron energization from magnetic reconnection in laser-driven plasmas. *Phys. Rev. Lett.* **116**, 095003 (2016).
18. Li, X., Guo, F., Li, H. & Li, G. Particle acceleration during magnetic reconnection in a low-beta plasma. *Astrophys. J.* **843**, 21 (2017).
19. Dahlin, J. T. Prospectus on electron acceleration via magnetic reconnection. *Phys. Plasmas* **27**, 100601 (2020).
20. Zenitani, S. & Hoshino, M. The generation of nonthermal particles in the relativistic magnetic reconnection of pair plasmas. *Astrophys. J. Lett.* **562**, L63–L66 (2001).
21. Egedal, J., Le, A. & Daughton, W. A review of pressure anisotropy caused by electron trapping in collisionless plasma, and its implications for magnetic reconnection. *Phys. Plasmas* **20**, 061201 (2013).
22. Drake, J. F., Swisdak, M., Che, H. & Shay, M. A. Electron acceleration from contracting magnetic islands during reconnection. *Nature* **443**, 553–556 (2006).
23. Hoshino, M., Mukai, T., Terasawa, T. & Shinohara, I. Suprathermal electron acceleration in magnetic reconnection. *J. Geophys. Res.* **106**, 25979–25998 (2001).
24. Savrukhin, P. V. Generation of suprathermal electrons during magnetic reconnection at the sawtooth crash and disruption instability in the T-10 tokamak. *Phys. Rev. Lett.* **86**, 3036–3039 (2001).
25. Klimanov, I., Fasoli, A. & Goodman, T. P., the TCV team. Generation of suprathermal electrons during sawtooth crashes in a tokamak plasma. *Plasma Phys. Control. Fusion* **49**, L1–L6 (2007).
26. DuBois, A. M. et al. Anisotropic electron tail generation during tearing mode magnetic reconnection. *Phys. Rev. Lett.* **118**, 075001 (2017).
27. Nilson, P. M. et al. Magnetic reconnection and plasma dynamics in two-beam laser-solid interactions. *Phys. Rev. Lett.* **97**, 255001 (2006).
28. Willingale, L. et al. Proton deflectometry of a magnetic reconnection geometry. *Phys. Plasmas* **17**, 043104 (2010).
29. Zhong, J. et al. Modelling loop-top X-ray source and reconnection outflows in solar flares with intense lasers. *Nat. Phys.* **6**, 984–987 (2010).
30. Fiksel, G. et al. Magnetic reconnection between colliding magnetized laser-produced plasma plumes. *Phys. Rev. Lett.* **113**, 105003 (2014).
31. E Raymond, A. et al. Relativistic-electron-driven magnetic reconnection in the laboratory. *Phys. Rev. E* **98**, 043207 (2018).
32. Gao, L. et al. Ultrafast proton radiography of the magnetic fields generated by a laser-driven coil current. *Phys. Plasmas* **23**, 043106 (2016).
33. Chien, A. et al. Study of a magnetically driven reconnection platform using ultrafast proton radiography. *Phys. Plasmas* **26**, 062113 (2019).
34. Chien, A. et al. Pulse width dependence of magnetic field generation using laser-powered capacitor coils. *Phys. Plasmas* **28**, 052105 (2021).
35. Dong, Q.-L. et al. Plasmoid ejection and secondary current sheet generation from magnetic reconnection in laser-plasma interaction. *Phys. Rev. Lett.* **108**, 215001 (2012).
36. Zhong, J. Y. et al. Relativistic electrons produced by reconnecting electric field in a laser-driven bench-top solar flare. *Astrophys. J. Suppl. Ser.* **225**, 30 (2016).
37. Wilks, S. C. et al. Energetic proton generation in ultra-intense laser–solid interactions. *Phys. Plasmas* **8**, 542–549 (2001).
38. Yamada, M. et al. Study of driven magnetic reconnection in a laboratory plasma. *Phys. Plasmas* **4**, 1936–1944 (1997).
39. Zhang, S. et al. Ion and electron acoustic bursts during anti-parallel reconnection driven by lasers. Preprint at https://arxiv.org/abs/2209.12754 (2022).
40. Phan, T. D. et al. Electron magnetic reconnection without ion coupling in Earth's turbulent magnetosheath. *Nature* **557**, 202–206 (2018).
41. Drake, R. P. et al. Efficient Raman sidescatter and hot-electron production in laser-plasma interaction experiments. *Phys. Rev. Lett.* **53**, 1739–1742 (1984).
42. Figueroa, H., Joshi, C., Azechi, H., Ebrahim, N. A. & Estabrook, K. Stimulated Raman scattering, two-plasmon decay, and hot electron generation from underdense plasmas at 0.35 μm. *Phys. Fluids* **27**, 1887–1896 (1984).
43. Ebrahim, N. A., Baldis, H. A., Joshi, C. & Benesch, R. Hot electron generation by the two-plasmon decay instability in the laser-plasma interaction at 10.6 μm. *Phys. Rev. Lett.* **45**, 1179–1182 (1980).
44. Uzdensky, D. Magnetic reconnection in extreme astrophysical environments. *Space Sci. Rev.* **160**, 45–71 (2011).
45. Cerutti, B., Werner, G. R., Uzdensky, D. A. & Begelman, M. C. Simulations of particle acceleration beyond the classical synchrotron burnoff limit in magnetic reconnection: an explanation of the Crab flares. *Astrophys. J.* **770**, 147 (2013).
46. Bowers, K. J., Albright, B. J., Yin, L., Bergen, B. & Kwan, T. J. T. Ultrahigh performance three-dimensional electromagnetic relativistic kinetic plasma simulation. *Phys. Plasmas* **15**, 055703 (2008).
47. Uzdensky, D. & Kulsrud, R. Physical origin of the quadruole out-of-plane magnetic field in Hall-magnetohydrodynamic reconnection. *Phys. Plasmas* **13**, 062305 (2006).
48. Birn, J. et al. Geomagnetic Environmental Modeling (GEM) magnetic reconnection challenge. *J. Geophys. Res.* **106**, 3715–3719 (2001).
49. Cassak, P., Liu, Y.-H. & Shay, M. A review of the 0.1 reconnection rate. *J. Plasma Phys.* **83**, 715830501 (2017).
50. Sharma Pyakurel, P. et al. Transition from ion-coupled to electron-only reconnection: basic physics and implications for plasma turbulence. *Phys. Plasmas* **26**, 082307 (2019).
51. Ji, H. & Daughton, W. Phase diagram for magnetic reconnection in heliophysical, astrophysical, and laboratory plasmas. *Phys. Plasmas* **18**, 111207 (2011).
52. Hillas, A. M. The origin of ultra-high-energy cosmic rays. *Annu. Rev. Astron. Astrophys.* **22**, 425–444 (1984).
53. Guo, F., Liu, Y.-H., Daughton, W. & Li, H. Particle acceleration and plasma dynamics during magnetic reconnection in the magnetically dominated regime. *Astrophys. J.* **806**, 167 (2015).
54. Vilmer, N. Solar flares and energetic particles. *Philos. Trans. R. Soc. A* **370**, 3241–3268 (2012).
55. Raymond, J. C., Krucker, S., Lin, R. P. & Petrosian, V. Observational aspects of particle acceleration in large solar flares. *Space Sci. Rev.* **173**, 197–221 (2012).

56. Goodman, J. & Uzdensky, D. Reconnection in marginally collisionless accretion disk coronae. *Astrophys. J.* **688**, 555–558 (2008).
57. Cangemi, F. et al. INTEGRAL discovery of a high-energy tail in the microquasar Cygnus X-3. *Astron. Astrophys.* **645**, A60 (2021).
58. Sari, R. & Piran, T. Predictions for the very early afterglow and the optical flash. *Astrophys. J.* **520**, 641–649 (1999).
59. Beloborodov, A. M. A flaring magnetar in FRB 121102? *Astrophys. J.* **843**, L26 (2017).
60. Torricelli-Ciamponi, G., Pietrini, P. & Orr, A. Non-thermal emission from AGN coronae. *Astron. Astrophys.* **438**, 55–69 (2005).
61. Massaro, F. & Ajello, M. Fueling lobes of radio galaxies: statistical particle acceleration and the extragalactic γ-ray background. *Astrophys. J. Lett.* **729**, L12 (2011).
62. Kataoka, J., Edwards, P., Georganopoulos, M., Takahara, F. & Wagner, S. Chandra detection of hotspot and knots of 3C 303. *Astron. Astrophys.* **399**, 91–97 (2003).

[1]Department of Astrophysical Sciences, Princeton University, Princeton, NJ, USA. [2]Princeton Plasma Physics Laboratory, Princeton University, Princeton, NJ, USA. [3]Department of Physics and Astronomy, University of Rochester, Rochester, NY, USA. [4]Laboratory for Laser Energetics, University of Rochester, Rochester, NY, USA. [5]Los Alamos National Laboratory, Los Alamos, NM, USA. [6]Lawrence Livermore National Laboratory, Livermore, CA, USA. [7]University of Michigan, Ann Arbor, MI, USA. [8]ELI-NP, 'Horia Hulubei' National Institute for Physics and Nuclear Engineering, Bucharest-Magurele, Romania. [9]University of Bucharest, Faculty of Physics, Bucharest-Magurele, Romania. [10]LULI-CNRS, CEA, UPMC Univ Paris 06: Sorbonne Université, École Polytechnique, Institut Polytechnique de Paris, Palaiseau Cedex, France. [11]University of Maryland, Baltimore County, Baltimore, MD, USA. [12]Institute of Laser Engineering, Osaka University, Osaka, Japan. ✉e-mail: achien@princeton.edu; hji@pppl.gov

Methods

Laser-powered capacitor coil target

Laser-powered capacitor coil targets are composed of parallel plates (capacitor) connected by one or multiple wires (coils). Holes are formed in the front (facing the driving laser) plate to allow the laser beam(s) to bypass the front plate and only hit the back plate. Suprathermal hot electrons are generated during the intense laser–solid interaction, some of which manage to escape from the back plate. A strong current is, therefore, supplied to the U-shaped wires from back to front, due to the resultant potential difference between the plates.

We use capacitor coil targets made from 50-μm-thick copper. The capacitors are formed by two square parallel plates with a length of 1.5 mm, with an interplate distance of 600 μm. Two holes with a radius of 250 μm are formed in the front plate to accommodate the OMEGA EP long-pulse beams 3 and 4. The plates are joined by one or two parallel U-shaped coils, with a rectangular cross section of 50 μm × 100 μm. Each coil consists of two 500 μm straight sections, joined by a semicircular section with a radius of 300 μm. In two-coil targets, the coils are separated by 600 μm. Capacitor coil targets are fabricated by laser cutting a design in 50-μm-thick sheet copper and then bending the coils into shape.

Particle spectra measurement using OU-ESM

The OU-ESM[63] is a time-integrated diagnostic that can provide angular resolution in either polar or azimuthal angles, relative to the target. This is accomplished by the use of five channels, each separated in angle by 5°. In the experiment, we chose the azimuthal angle spread, since this pitch angle allows for distinguishing between acceleration mechanisms in an axisymmetric setup, with symmetry in the polar direction.

After reaching the spectrometer, an electron first passes through a pinhole 700 μm wide and 2 cm deep. The separation of electron energies is accomplished with a set of permanent magnets placed along the detector line of sight, creating a magnetic field perpendicular to the line of sight. The $\vec{v} \times \vec{B}$ force deflects differently energized electrons to different distances along the detector length onto a BAS-TR image plate. In general, impacts closer to the detector entrance represent lower-energy electrons. In the experiment, magnets were chosen corresponding to electron energies in the 20 keV to 1 MeV range.

The field of view and solid angle subtended by each channel are defined by the pinhole size $p = 700$ μm, distance to target $D = 37.5$ cm and pinhole/collimator depth $d = 2$ cm. The field of view is given by $\mathrm{FOV} = pD/d = 13.1$ mm, which is much larger than the target size and sufficient to capture electrons from the main interaction. The solid angle can be approximated by $\Omega \approx p^2/D^2 = 3.5 \times 10^{-6}$ sr and provides the primary restriction for electrons reaching the detector.

The primary sources of error in interpreting the OU-ESM data involve the image-plate response to energetic electrons and image-plate scanning offsets. The image-plate response is taken from another work[64], and introduces a 28% uncertainty. In addition, image-plate signals decay with time; therefore, image plates are scanned at exactly 30 min after the shot for consistency in signal level. In interpreting the image plate, defining the edge of the magnets is critical to an accurate energy spectrum. Here an uncertainty of approximately 5 pixels or 0.5 mm is introduced, translating to an uncertainty in the spectrum energy.

Plasma parameter measurements using Thomson scattering

Plasma parameters, such as electron temperature and densities, are characterized by the collective Thomson scattering of the 527 nm probe laser. The probe is focused on the plasma 600 μm above the X line of the reconnection plane (Fig. 1a). The scattered light in a volume of $60 \times 60 \times 50$ μm^3 is collected by an $f/10$ reflective collection system[65], and the scattering angle is 63.4°. The collected scattered light is temporally and spectrally resolved by narrowband (7 nm window for ion acoustic waves) and broadband (320 nm window for electron plasma waves) spectrometers, coupled with streaked cameras with a 5 ns streak window. The electron temperature and density are obtained by forward fitting the synthetic spectrum to the experimentally measured broadband spectrum averaged over a 0.1 ns window.

PIC simulation setup

The 2D PIC simulation box has dimensions of $L_z = 4D_{\mathrm{coil}}$ and $L_R = 2D_{\mathrm{coil}}$ in the z and R directions, respectively, where D_{coil} is the intercoil distance of 600 μm. To avoid the difficult boundary at $R = 0$, a minimum radius of $R_{\mathrm{min}} = 50$ μm was used. Two rectangular-cross-section coils of width $l_z = 100$ μm and height $l_R = 50$ μm are located at $R = R_{\mathrm{coil}} = 300$ μm and $z = \pm D_{\mathrm{coil}}/2 = \pm 300$ μm, matching the experimental positions.

In the simulation, lengths are normalized to electron skin depth $d_{\mathrm{e}} = c/\omega_{\mathrm{pe}}$, and times are expressed in terms of the inverse electron plasma frequency $\omega_{\mathrm{pe}}^{-1}$. Due to the large Lundquist number, collisions are turned off in the simulation.

It is computationally untenable to perform a simulation with completely physical parameters, and so, priorities must be made. An accurate particle spectrum is of great importance, so reducing the ion-to-electron mass ratio $m_{\mathrm{i}}/m_{\mathrm{e}}$ is undesirable. In addition, the β value of plasma has been shown to be a critical parameter in particle acceleration[66], so we maintain the physical β value in the simulation. To reduce computational time, we instead use artificially small values of the electron plasma frequency to electron gyrofrequency $\omega_{\mathrm{pe}}/\Omega_{\mathrm{ce}}$. By keeping β constant, a reduced $\omega_{\mathrm{pe}}/\Omega_{\mathrm{ce}}$ represents an artificially strong magnetic field, coupled to an artificially hot plasma. Scaling relations for electromagnetic field strength can be established as a function of $\omega_{\mathrm{pe}}/\Omega_{\mathrm{ce}}$ to extrapolate to physical conditions. The physical $\omega_{\mathrm{pe}}/\Omega_{\mathrm{ce}} = 6.33$, and simulations are run for reduced values of $\omega_{\mathrm{pe}}/\Omega_{\mathrm{ce}} = 6.33/3$, 6.33/4, 6.33/6, 6.33/12, 6.33/16 and 6.33/24.

Cell size is limited by the Debye length, so the number of cells changes with $\omega_{\mathrm{pe}}/\Omega_{\mathrm{ce}}$. At $\omega_{\mathrm{pe}}/\Omega_{\mathrm{ce}} = 6.33/4$, the number of cells is $n_z \times n_R = 1{,}440 \times 720$, spanning $L_z \times L_R = 451.6d_{\mathrm{e}} \times 225.8d_{\mathrm{e}}$. Here 200 macroparticles of each species are initialized per cell. The achievable cell size and number of macroparticles per cell also limit a viable scaling of accelerated electron spectra to be established for the small electron diffusion region where electrons are demagnetized and thus are free to be accelerated by the reconnection electric field.

For physical $\omega_{\mathrm{pe}}/\Omega_{\mathrm{ce}} = 6.33$, the simulation is initialized with a uniform Maxwellian plasma with $n_{\mathrm{e}} = 10^{18}$ cm^{-3}, $n_{\mathrm{i}} = n_{\mathrm{e}}/Z = 5.6 \times 10^{16}$ cm^{-3}, $T_{\mathrm{e}} = T_{\mathrm{i}} = 400$ eV to match the experimental parameters. Compared with experiment, a lower initial plasma density is used due to the inclusion of a particle injection scheme from the coil region. A representative magnetic field strength $B_0 = 50.7$ T is taken to be the upstream magnetic field at $z = -D_{\mathrm{coil}}/4$ from the centre between the coils. The simulation β value is, therefore, 0.063. Due to the artificially reduced $\omega_{\mathrm{pe}}/\Omega_{\mathrm{ce}}$ values, the ion and electron temperatures and coil magnetic fields are artificially increased, and the density is kept constant to maintain the β value of plasma.

Electrically conducting boundary conditions are set for fields, and open-boundary conditions[67] are set for particles in the z and R directions (periodic boundary conditions are set for θ). The open-boundary conditions prevent accelerated particles that would otherwise escape the system from being re-accelerated. Our choice, therefore, prevents an overestimation of particle acceleration that would be inevitable with periodic or reflecting boundaries.

At $t = 0$, electromagnetic fields are set to 0. The capacitor coil currents are modelled by injecting currents with the following time profile:

$$I_{\mathrm{coil}}(t) = \begin{cases} I_0(t/t_{\mathrm{rise}}), & t < t_{\mathrm{rise}} \\ I_0 \exp(-(t - t_{\mathrm{rise}})/t_{\mathrm{decay}}), & t \geq t_{\mathrm{rise}} \end{cases} \quad (1)$$

where $t_{\mathrm{rise}} = 1.0$ ns, $t_{\mathrm{decay}} = 8.6$ ns and $I_0 = 57$ kA match the experimental measurements. Currents are oriented into the page ($-\theta$ direction). The coil magnetic fields are then calculated from the current distribution within the coils.

The reconnection plasma primarily emanates from the coils, due to the ablation of copper plasma by ohmic heating within the coils and irradiation by X-rays from the laser interaction. In contrast, the plasma generated at the laser spot takes a few nanoseconds to flow into the reconnection region, and does not play an important role in reconnection, particularly during the push phase. To simulate the coil plasma, we use a particle injection scheme: a volume injector is implemented around the coils, with a Gaussian spatial profile (Gaussian width and height are set to l_z and l_R, respectively), and a linear time dependence from $t = 0$ to $t = 1$ ns. The injection rate is tuned to match the experimental density measurements. Without the particle injection scheme, density voids form around the coils when the strong magnetic field pressure pushes out plasma as the magnetic field diffuses outwards from the coils.

Proton ray tracing using PIC electromagnetic fields

Protons are advanced through a three-dimensional (3D) representation of the PIC fields through a fourth-order Runge–Kutta algorithm. Electric and magnetic fields are applied onto a 3D grid by projecting from a 2D simulation using the following methodology:

1. The centre of the semicircular coil is defined as the origin. For each proton near the coil region, the radius and azimuthal angle relative to the topmost point of the coil are calculated ($\theta = 0$ corresponds to the 'vertical' reconnection plane).
2. For angles corresponding to the lower hemisphere ($\theta > 90°$ or $\theta < -90°$), electromagnetic fields are assumed to be 0.
3. If the proton is sufficiently far away from the coils to be outside the effective PIC simulation box ($r > R_{\mathrm{PIC,max}}$ or $r < R_{\mathrm{PIC,min}}$), electromagnetic fields are assumed to be 0.
4. The 3D electric and magnetic fields corresponding to the radial and axial positions in the reconnection plane are found with linear interpolation.
5. These fields are rotated by the azimuthal angle that corresponds to the proton location.

Simply, the 2D reconnection plane is 'swept' in angle along the semicircular portion of the coils. For each synthetic radiograph, 10^7 protons are sampled, with a maximum source angle of 0.4 rad. The 'impact coordinates' of each proton at a predefined synthetic detector are combined into a 2D histogram, spanning $L_y = L_x = 2.46$ mm in both directions with 500 bins in each direction. Each bin, thus, represents a 4.9 μm width.

LPI-generated electron deflections by coil magnetic fields

The angular dependence of accelerated electrons measured by OU-ESM was interpreted as evidence of electrons accelerated by the reconnection electric field. However, this interpretation does not take into account the possibility of LPI-generated electrons being preferentially deflected by coil magnetic fields in certain angles, resulting in the measured angular distribution in the electron energy spectra. To explore this possibility, numerical ray tracing is performed using positrons advanced through the vacuum-coil magnetic field.

Instead of advancing electrons from the laser spot to the electron spectrometer, positrons are initialized at the spectrometer, and advanced towards the capacitor coil target. Due to charge–parity–time symmetry, a positron advancing 'backward' in time through electromagnetic fields is equivalent to an electron advancing 'forward' in time through the same fields. These two simulations are, thus, functionally similar, but the former allows for substantially faster computation times due to more limited angular spread around the collimator at the OU-ESM. Positron ray tracing is performed for all the five OU-ESM channels. Positrons with a kinetic energy of 50 keV are initialized at the entrance of each channel, with an angular spread of 1° in both polar and azimuthal angles, providing a field of view that adequately encompasses the entire capacitor coil target. These positrons are then advanced through the vacuum magnetic fields calculated from the coil current geometry via a fourth-order Runge–Kutta algorithm. The majority of these positrons leave the field region, but the few that impact the capacitor coil plates are recorded. In addition to scanning across the OU-ESM channel angles, the ray tracing is scanned across various coil currents, from 0 kA, up to the maximum coil current of 57 kA, and three different coil configurations: double coil (reconnection), left coil only (control) and right coil only (control). For each combination of OU-ESM channel, coil current and coil configuration, 5×10^5 positrons are used.

In all the coil configurations, positrons are only deflected towards the laser spot (defined as a 50-μm-radius circle centred on the back plate) for small finite coil currents of $0 < I \lesssim 3$ kA. For larger coil currents ($I \gtrsim 5$ kA), the positrons are completely deflected away from the back plate, with no deposited positrons recorded. For $I \lesssim 5$ kA, the deposition pattern of positrons is seen to move 'downward' with an increasing coil current. This is explained by the $\vec{v} \times \vec{B}$ force from the 'horizontal' magnetic field (Fig. 1b, left to right).

An interesting trend appears when comparing the double-coil reconnection configurations with either right- or left-coil control configurations (Extended Data Fig. 1a). Across all the channels, the right- and left-coil configurations (Extended Data Fig. 1a, dashed and dotted lines, respectively) result in more positrons deflected near the laser spot than the double-coil configuration (Extended Data Fig. 1a, solid lines). Reverting to the electron frame, this implies that LPI-generated electrons with energies of 50 keV are less likely to be deflected towards the electron spectrometer by double-coil configurations compared with single-coil configurations. The possibility of the double-coil case acting as an 'energy selector' causing the spectral bumps is, therefore, small. Furthermore, we have shown that 50 keV electrons are deflected towards the OU-ESM for a very limited range of coil currents, compared with the maximum coil current of 57 kA. As OU-ESM is a time-integrated diagnostic, even if some sort of energy selection mechanism were to exist, the effect on the entire spectrum would be small, as the coil current spends comparatively little time in the $0 < I \lesssim 3$ kA range.

The model is not perfect, primarily due to the assumption of vacuum magnetic fields and the ignoring of plasma effects. The relative importance of plasma effects in the exercise can be illustrated by the no-coil experimental spectra shown in Fig. 2f. Without plasma effects, no LPI electrons are expected at the OU-ESM, as the field of view of the instrument does not include the laser spot from which LPI electrons originate. The low signal level of the measured no-coil spectra, therefore, illustrates the relative insignificance of plasma effects on the measured and simulated electron spectra. Despite the assumptions, the overall exercise does not support an energy selection mechanism, whereby LPI-generated electrons of ~50 keV energy are deflected by coil magnetic fields alone and are responsible for the spectral bump.

As electron/positron deflections by magnetic fields are dependent on the particle energy, it is important to not focus only on one particular energy. Instead, the spectrum shape as a function of particle energy can be modelled. Taking the initial electron distribution from the no-coil experimental spectra, positron ray tracing is performed for the range of positron energies from 20 to 100 keV in 10 keV increments, and keeping coil current constant at 1 kA. As shown in Extended Data Fig. 1a, for each originating channel, the number of positrons collected at the laser spot is plotted for each positron energy. The resultant simulated spectra (Extended Data Fig. 1b), therefore, represents the no-coil electron spectra 'transformed' by the vacuum-coil magnetic fields in a double-coil configuration. By comparing these simulated spectra with the two-coil spectra (Fig. 2a–c), we observe simulated spectral dips in the 30–50 keV energy range, which are inconsistent with the experimental spectral bumps in the 40–70 keV energy range. This inconsistency shows that the experimental spectral bumps cannot be adequately explained with vacuum magnetic fields alone deflecting LPI-generated electrons towards different detector channels.

The same ray-tracing method can be used to demonstrate the energy selection mechanism that causes the low-energy deficiency in channels 4 and 5 in the left-coil experimental spectra (Fig. 2e). The simulated left-coil spectrum is shown in Extended Data Fig. 1c. Due to a larger deflection on low-energy particles, relatively fewer positrons originating from channels 4 and 5 are observed at the laser spot, compared with high-energy particles. The effect is evident in the ray-tracing spectra, and explains the low-energy interchannel behaviour in the experimental data.

Data availability

Data are available from the corresponding authors upon reasonable request.

Code availability

Information about the VPIC code is available via GitHub at https://github.com/lanl/vpic. Data analysis code is available from the corresponding authors upon reasonable request.

References

63. Habara, H. et al. A ten-inch manipulator (TIM) based fast-electron spectrometer with multiple viewing angles (OU-ESM). *Rev. Sci. Instrum.* **90**, 063501 (2019).
64. Bonnet, T. et al. Response functions of imaging plates to photons, electrons and ^{4}He particles. *Rev. Sci. Instrum.* **84**, 103510 (2013).
65. Katz, J. et al. A reflective optical transport system for ultraviolet Thomson scattering from electron plasma waves on OMEGA. *Rev. Sci. Instrum.* **83**, 10E349 (2012).
66. Li, X., Guo, F., Li, H. & Birn, J. The roles of fluid compression and shear in electron energization during magnetic reconnection. *Astrophys. J.* **855**, 80 (2018).
67. Daughton, W., Scudder, J. & Karimabadi, H. Fully kinetic simulations of undriven magnetic reconnection with open boundary conditions. *Phys. Plasmas* **13**, 072101 (2006).

Acknowledgements

This work was supported by the Department of Energy (DOE) Office of Science, Fusion Energy Sciences (FES), under the LaserNetUS initiative at the Jupiter Laser Facility and OMEGA Laser Facility. This work was mainly supported by the High Energy Density Laboratory Plasma Science program by Office of Science and NNSA under grant no. DE-SC0020103 (H.J., A.C., L.G., S.Z. and E.G.B.), and also by DOE grants GR523126 and NSF grant PHY-2020249 (E.G.B.). We express our gratitude to General Atomics, the University of Michigan and the Laboratory for Laser Energetics for target fabrication, and to the Jupiter Laser Facility, OMEGA and OMEGA EP crews for experimental and technical support. H.J. thanks M. Yamada, J.-Y. Zhong, S. Prager, C. Ren, K. Huang and Q.-M. Lu for their contributions during initial development of this project.

Author contributions

H.J., L.G. and E.G.B. initiated the research. A.C., L.G., S.Z., H.J. and E.G.B. designed the experiments. A.C., L.G., S.Z., H.J., R.F., H.C., G.F., G.B., R.C.C., S.N.C., A.F., K.F., O.F., D.H.F., J.F., S.F., K.H., A.R. and R.T performed the experiments, with target support by S.K. and C.K. A.C. performed the PIC simulations, with major support from W.D., A.S., A.L. and F.G. A.C. performed the ray-tracing calculations. A.C., L.G., S.Z., H.J. and E.G.B. contributed to the experimental data analysis, as well as interpretation and physics discussions of the simulation results. H.J. and E.G.B. contributed to the astrophysical implications. A.C., L.G., S.Z., H.J. and E.G.B. wrote and revised the main paper. All the authors read and approved the final manuscript.

Competing interests

The authors declare no completing interests.

Additional information

Extended data is available for this paper at https://doi.org/10.1038/s41567-022-01839-x.

Supplementary information The online version contains supplementary material available at https://doi.org/10.1038/s41567-022-01839-x.

Correspondence and requests for materials should be addressed to Abraham Chien or Hantao Ji.

Peer review information *Nature Physics* thanks Anabella Araudo and the other, anonymous, reviewer(s) for their contribution to the peer review of this work.

Reprints and permissions information is available at www.nature.com/reprints.

https://doi.org/10.1038/s41567-022-01839-x

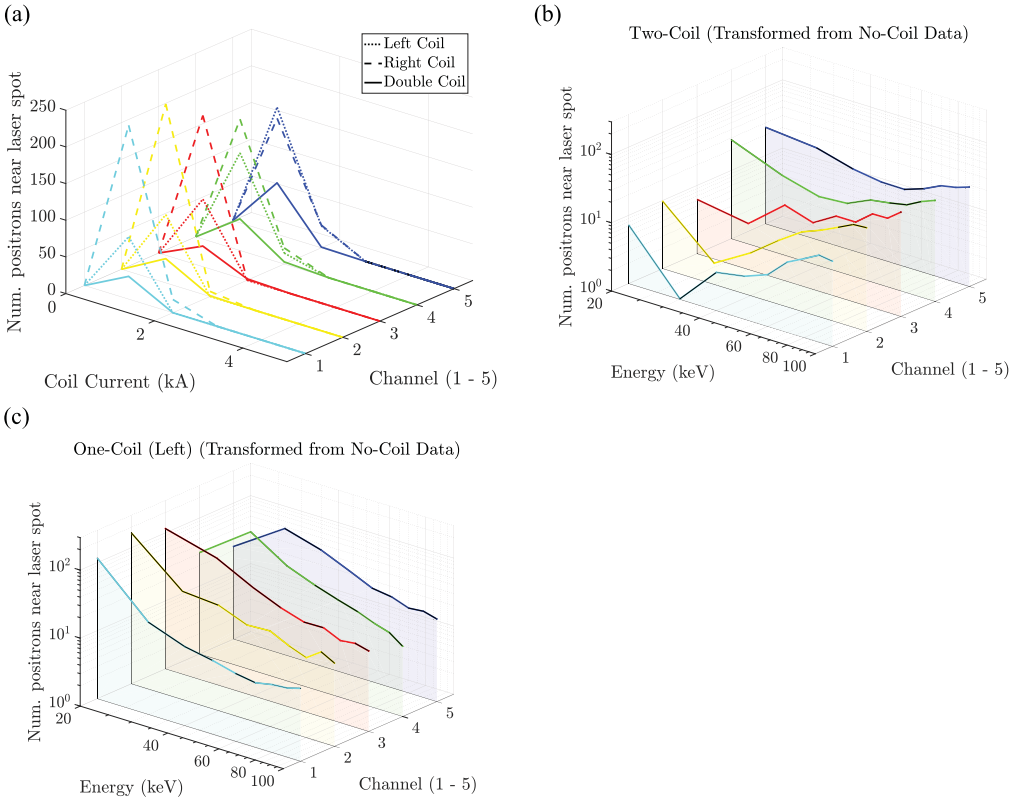

Extended Data Fig. 1 | Positron raytracing with vacuum coil magnetic fields without reconnection. a, The number of positrons near the laser spot are plotted as a function of OU-ESM channel, coil configuration, and coil current. In all coil configurations, positrons are deflected near the laser spot only for small finite coil currents $0 < I \lesssim 3$kA, as larger coil currents deflect the positrons below the bottom of the back plate. Further, across all channels, left and right coil configurations consistently exhibit larger positron impacts than the double coil configuration. This exercise implies that LPI-generated electrons are unlikely to be preferentially accelerated to the OU-ESM by double coil magnetic fields, as compared to single coil magnetic fields. **b**, A simulated five-channel energy spectrum is generated by transforming the experimental no-coil spectrum via positron raytracing at energies of 20 – 100keV, in 10keV increments. The applied magnetic field is the two-coil configuration, with a constant coil current of $I = 1$kA. Across all channels, simulated spectral dips are observed at 30 – 50keV, in contrast with the experimental spectral bumps (Fig. 2a,b,c) at 40 – 70keV. **c**, Application of the same raytracing technique to the left-coil configuration can demonstrate the selection mechanism at low energies in Channels 4 and 5, as described in the Fig. 2e caption. In the raytracing spectrum, dips are observed at low energy in Channels 4 and 5, as the lower-energy positrons are preferentially deflected to large $\theta - z$ angle by the coil magnetic field.